1-1-2009

Quantitative Imaging of Scattering Changes Associated with Epithelial Proliferation, Necrosis and Fibrosis in Tumors Using Microsampling Reflectance Spectroscopy

Venkataramanan Krishnaswamy
Dartmouth College

P Jack Hoopes
Dartmouth College

Kimberley S. Samkoe
Dartmouth College

Julia A. O'Hara
Dartmouth College

Tayyaba Hasan
Wellman Center for Photomedicine

See next page for additional authors

Authors
Venkataramanan Krishnaswamy, P Jack Hoopes, Kimberley S. Samkoe, Julia A. O'Hara, Tayyaba Hasan, and Brian W. Pogue

Published in final edited form as:
J Biomed Opt. 2009 ; 14(1): 014004. doi:10.1117/1.3065540.

Quantitative Imaging of Scattering Changes Associated With Epithelial Proliferation, Necrosis and Fibrosis in Tumors Using Microsampling Reflectance Spectroscopy

Venkataramanan Krishnaswamy[†], **P. Jack Hoopes**[†,‡], **Kimberley S. Samkoe**[†], **Julia A. O'Hara**[‡], **Tayyaba Hasan**[*,+], and **Brian W. Pogue**[†,‡,*]

[†]Thayer School of Engineering, Dartmouth College, Hanover, NH 03755.

[‡]Department of Surgery, Dartmouth Medical School, Hanover, NH 03755.

[*]Wellman Center for Photomedicine, Massachusetts General Hospital, MA 02114.

[+]Department of Dermatology, Harvard Medical School, MA 02115.

Abstract

Highly localized reflectance measurements can be used to directly quantify scatter changes in tissues. This study presents a microsampling approach that is used to raster scan tumors to extract parameters believed to be related to the tissue ultra-structure. A confocal reflectance imager was developed to examine scatter changes across pathologically distinct regions within tumor tissues. Tissue sections from two murine tumors, AsPC-1 pancreas tumor and the Mat-LyLu Dunning prostate tumor, were imaged. After imaging, histopathology-guided region-of-interest studies of the images allowed analysis of the variations in scattering resulting from differences in tissue ultra-structure. On average, the median scatter power of tumor cells with high proliferation index was about 26% less compared to tumor cells with low proliferation index (LPI). Necrosis exhibited the lowest scatter power signature across all the tissue types considered, with about 55% lower median scatter power than LPI tumor cells. Additionally, the level and maturity of the tumor's fibroplastic response was found to influence the scatter signal. This approach to scatter visualization of tissue ultra-structure *in situ* could provide a unique tool for guiding surgical resection, but this kind of interpretation into what the signal means relative to the pathology is required before proceeding to clinical studies.

Introduction

One of the significant challenges during surgery is the lack of obvious contrast between normal and tumor tissues in the margins of many invasive tumors. While surgical microscopes can be fitted with color filtering [1, 2], polarizers [3, 4] or spectroscopic channels [5], there is still room for definition of tools which would provide better delineation of the tissue ultra-structure *in situ* and can readily gain clinical adoption. One key area of work is in the idea of decoupling the signal scatter from absorption *in situ*, which would be extremely beneficial, since the origin of absorption signals is thought to be completely separate from the features causing scatter [6-9]. Several techniques exist for imaging features related to scatter using reflectance polarization [3, 10-13], yet comparatively less attention has been paid to imaging the scatter spectrum directly. There have been some unique designs for novel optical fiber based probes [14-17], which have potential to guide biopsy or provide differential information about tissue status, and extending the signal processing of these devices into an imaging mode would be quite beneficial. This paper looks at one approach to broadband spectral reflectance imaging to quantify scatter in an imaging geometry, where the field of view is large enough to allow eventual translation as a surgical pathology aid. In addition, the approach allows easy quantification of the scattering

coefficient heterogeneity within tissue samples and this information is critical to treatment planning in optical treatment such as photodynamic therapy [18-20].

Scatter analysis of cells and tissues has provided some fundamentally exciting potential in recent years. Angle resolved or coherence based reflectance methods have been shown to allow quantification of the scatter origin features in tissue [17, 21-25], which can be robust measures of pathologic change. The shape and size of scattering features can produce resonances in the angularly resolved emission or in the wavelength resolved emission, which could be extracted from the overall spectral data. The techniques that are based on locally resolved reflectance measurements are well studied, but have not been extended into imaging systems. Since these methods have been shown to work for quantifying scatter and absorption changes in tissue if the target optical properties are within a typical range observed in tissue, they are ideal for extension to imaging, if a reasonable way can be found to measure scatter in small regions such as 100 micron diameter, which is equivalent to approximately one mean scattering length in tissue [26-30]. The logical approach to this is to develop a raster scanning system that takes full broadband wavelength data as reflected from the tissue surface. The optical design constraints on this system are many, in that with broadband light the optics have to be chromatically corrected and work quickly enough to allow capture of the broadband data at every pixel.

A new raster-scanning reflectance imager has been designed here, based on these techniques to directly quantify tissue scatter changes *in situ*. The system is outlined and the features of the detected scatter signals are analyzed with two tumor models, looking at the variation in scattering parameters within the tumor line. The system has good potential for extension to clinical imaging, but the heterogeneity observed in real tumor tissue can be enormous, and so this study focuses on classifying the signal types obtainable from localized scatter, and directly comparing them to what is seen by a pathologist. The ability to use this data for diagnostic studies and treatment planning is discussed.

Materials and Methods

Scatter Imaging System

The scatter imaging system primarily consists of a confocal spectroscopic system having 100 micron illumination spot size and a raster-scanning sample platform built using linear translation stages. The optical and electromechanical subsystems are integrated via a custom developed LabVIEW (National Instruments, Austin, TX) interface. Figure 1 shows the schematic of this system, which resembles a traditional confocal microscope, but is designed to directly image scatter from tissue. This is achieved by ensuring the illumination and detection spot sizes on the tissue surface are less than one scattering length (typically 100 μm for tissue) [27] over the entire waveband of interest. In this regime the incident photons are predominantly singly scattered and the detected signal is largely independent of local absorption.

The illumination optics train consisted of a 50 μm core fiber (F1) coupled to a 20 W tungsten-halogen white light source (HL-2000-HP, Ocean Optics Inc., Dunedin, FL) placed at the front focal point of an achromatic lens (L1) (PAC040, Newport Corporation, Irvine, CA). A 10X, 0.28 NA, long working distance, air immersion, plan-apochromatic objective (L2) was used to refocus the light on to the sample plane. The illumination optics train was modeled in ZEMAX© optical design software (version July 22, 2004, ZEMAX Development Corporation, Bellevue, WA) to make sure the illumination spot size was less than 100 μm over the entire wavelength band used. The 50μm diameter extended source (fiber core) was modeled as a collection of point sources placed at the extremities of the source field positions. The transverse magnification of the illumination optics train was approximately 0.4. The theoretical spot size at the sample plane was found to be less than approximately 40 μm over a broad wavelength range of 450 nm to 800 nm, with chromatic aberration dominating the point spread function.

The theoretical spot size was within 100 μm for a depth of approximately 130 μm on either side of the best focus plane. It should be noted that the microscope objective (L2) lens system was modeled as a single paraxial lens with equivalent specifications as the actual lens data for the objective was not available. However, the objective is well corrected for common optical aberrations and was expected to deliver a diffraction-limited performance over the design waveband. The spot size was also experimentally measured using the standard knife edge technique and was found to be approximately 89 μm.

The detection optics train used the same microscope objective to pick-up the backscattered light from the sample and a 50/50 beam splitter (BS) was used to separate the illumination and detection beam paths. Another achromatic lens (L3) was used to focus the detected photons on to the proximal face of a 100 μm core detection optical fiber (F2) which also acted as the confocal pinhole. The size of the detection spot on the target was controlled by the detection fiber's core diameter and the lateral magnification of the optical system. The detection optical train provided a magnification of approximately 2.5 and thus the 100 μm detection fiber picked up light from a 40 μm region overlapping the illumination spot on the sample plane. The distal end of the detection fiber is coupled to an imaging spectrometer (SpectraPro 2156, Princeton Instruments Inc., Trenton, NJ) with a 150 grooves/mm, 500 nm blaze wavelength, ruled grating and a 16-bit, thermo-electrically cooled Cascade 512F EM-CCD (Princeton Instruments Inc., Trenton, NJ). The CCD has a field of 512×512 pixels with a pixel size of 16 microns. The spectrometer was calibrated using characteristic spectral lines from a calibrated fluorescent lamp PLS 11W/827 (Philips Lighting, Somerset, NJ)[31] to operate in the wavelength range of 510 nm-785 nm that encompasses the strong hemoglobin absorption peaks. The spectral resolution was approximately 1 nm.

A custom sample mount was designed to hold removable microscope slides and standard 96-well plates for tissue and liquid phantom measurements, respectively. The mount was integrated into a XY linear translation platform and aligned such that the top surface of the microscope slide lies exactly on the focal plane of the objective lens (L2). The entire optical head was mounted on a vertical translation stage to enable the scan spot to move in and out of the sample plane to allow for precise vertical alignment.

At normal incidence, Fresnel reflections off the glass-sample interface can cause significant measurement artifacts, so the sample plane was tilted by about 45° with respect to the optical axis to prevent specular reflections from entering the detection path. A significant portion of the illumination beam still coupled into the detection path and was found to be due to Fresnel reflection from one of the beam splitter faces. This signal however remained constant during the measurement process and was mathematically removed by measuring a background spectrum, $I_{bg}(\lambda)$, with no sample present. A block of Spectralon™ (Labsphere Inc, North Sutton, NH), a spectrally flat thermoplastic resin, was used to collect a reference spectrum, $I_{ref}(\lambda)$. At each pixel location, the remitted scatter spectrum (I_R) was calculated by dividing the measured spectrum (I_{meas}) by the reference spectrum (I_{ref}) to remove the instrumental spectral response as shown in the equation,

$$I_R(\lambda) = \frac{I_{meas}(\lambda) - I_{bg}(\lambda)}{I_{ref}(\lambda) - I_{bg}(\lambda)}. \quad (1)$$

The raster-scanning and spectral acquisition sequence is synchronized and controlled by a custom developed LabVIEW front-end. The scan length is limited to 25.4 mm in both directions providing a full field capability of 254×254 pixels at 100 μm resolution.

Parameter Fitting

In the absence of significant local absorption, the relationship between the measured irradiance and wavelength would be approximated by a power law type empirical relation,

$$I_R(\lambda) = A\lambda^{-b}, \tag{2}$$

where, *A* is the scattered amplitude and *b*, the scattering power. However in the presence of significant local absorption, for very small source-detector separations, an empirical relationship can be used to estimate the spectral reflectance,

$$I_R = A\lambda^{-b} \exp\left(-kc\left(d\left(HbO2(\lambda)\right) + (1-d)\,Hb(\lambda)\right)\right), \tag{3}$$

if scattering and absorption coefficients are within the typical range found in tissue [29, 30]. Parameter *c* is proportional to the concentration of whole blood, *k* is the path length and *d* is the hemoglobin oxygen saturation fraction. The extinction spectra of oxygenated and deoxygenated hemoglobin, *HbO2* and *Hb*, were obtained from the Oregon Medical Laser Center database[32]. This data has a spectral resolution of 2 nm and a standard piecewise cubic Hermite interpolation polynomial was used to estimate extinction values for wavelengths in-between. Since the absorption from other chromophores is minimal in the waveband of interest, their contributions were assumed to be negligible.

The spatial extent of illumination and detection was less than one mean free path length of interaction (typically 100 μm), so the detected photons are thought to be predominantly singly scattered and the measured spectrum is independent of local absorption. However in regions where high local concentration of chromophores is encountered, like regions with blood pooling or high vascularity, this approximation is not valid and a correction for absorption is required to describe the scatter spectrum accurately. The exponential term in Equation 3 serves as this correction factor with the empirical fitting process providing an estimate on the product of the path length and the whole blood concentration, ‘kc’, and the hemoglobin oxygen saturation fraction ‘d’. It should be noted that, in this probe geometry, it is not possible to decouple the path length ‘k’ and the absolute chromophore concentration ‘c’ from the measured spectra.

Another parameter of interest is the average scattered irradiance, I_{avg}, integrated over all wavelengths, and given mathematically by,

$$I_{avg} = \int_{\lambda_1}^{\lambda_2} I_R(\lambda)\, d\lambda. \tag{4}$$

Only a subset of the measurement waveband, from 610 nm to 785 nm, was considered for computing I_{avg}, where absorption due to hemoglobin, the dominant chromophore, is minimal. This parameter provides a quick and direct estimate of average scatter without the need for an empirical model, and is directly proportional to the irradiance which would be detected by a simple camera without wavelength filtering.

Animals

All animals were housed in the animal facility with 12 h light–dark cycles, with temperature control, free access to water and standard laboratory diet. All procedures and experiments were approved by the Animal Care and Use Committee of Dartmouth College.

Prostate Tumors

Orthotopic prostate tumors were grown in male Copenhagen rats (average 120–150 g body weight, Charles River Laboratories, Wilmington, MA)[33]. For all procedures, the rats were anesthetized with an intramuscular injection of a mixture of ketamine and xylazine (90:9 mg/kg). For orthotopic implants, the rat abdominal area and hind flanks were shaved and prepared in an aseptic surgical manner. R3327 MatLyLu Dunning prostate cancer cells[34] were cultured in RPMI 1640 with glutamine (Mediatech, Herndon, VA) supplemented with 10% fetal bovine serum (HyClone, Logan, UT) and 100 units/mL penicillin-streptomycin (Mediatech, Herndon, VA). The tumor was induced by injection of 1×10^5 cells on the right flank in 0.05 mL sterile phosphate buffered saline (PBS). Tumor growth was assessed by external measurements with calipers, three times per week. Tumors were used for the experiment at 9 to 12 days after inoculation, with a surface diameter of 7 to 9 mm and a thickness of 2 to 4 mm.

Pancreatic Tumors

For the subcutaneous pancreatic tumors, male C.B.-17 strain 236 SCID mice (6-7wks, Charles River Laboratories, Wilmington, MA) were used. Human pancreatic tumor cells, AsPC-1 were grown and maintained in RPMI 1640 with 2 mM L-glutamine with 25 mM HEPES (Lonza, Walkersville, MD), and 1.0 mM sodium pyruvate and fetal bovine serum, 10% (Atlanta Biologicals, Lawrenceville, GA), with 100 units/mL of penicillin-streptomycin (Mediatech, Herndon, VA). Tumors were induced by injecting 1×10^6 AsPC-1 cells (50 μL volume) subcutaneously in the flank region. Cells were suspended in a solution of 50% culture medium (without FBS) and 50% Matrigel (BD Biosciences, Bedford, MA), loaded into insulin syringes and were kept on ice until they were injected under the skin. Tumors were measured (calipers) weekly throughout the seven week study. When harvested for this experiment, the tumors measured 6-7 mm in diameter and 5-6 mm in thickness.

Tumor Imaging

Excised whole tumors were dissected into 4-5 mm thick sections and imaged using the scatter imaging system. The scan resolution was maintained at 100 μm, and the measurements were referenced to a Spectralon standard as before. The sample was held inside a rubber gasket, and sandwiched between two glass slides with the imaged surface facing down. This arrangement kept the sample in a reasonably air-tight environment and also ensured that a flat surface was presented to the scanning beam. The scanning sample stage took approximately 1 hour to scan the entire field of interest. A few drops of PBS were placed on the sample before the start of the scan to prevent it from drying during the measurements. Addition of PBS did not alter the signal in a significant manner. It was assumed that the sample optical properties did not change significantly during the measurement process. After the measurement the sample was immediately placed in 4% neutral buffered formaldehyde solution for fixation and routinely processed for histology evaluation. All histology sections were superficially cut at 4μm and stained with hematoxylin and eosin (H&E) for imaging analysis.

Histopathology Classification of Tumor Sub-Regions

A veterinary pathologist (P. J. H.) examined the H&E sections from each sample and identified several regions-of-interest corresponding to the tissue types observed. The tissue types observed across all samples were classified under three major groups with constituent subgroups as listed in Table 1. The epithelial group was identified as containing two distinct types of epithelial cells, one that exhibited higher nucleus to cytoplasm ratio compared to the other. As higher nucleus to cytoplasm ratio is indicative of cell proliferation the subgroup containing this type of cells was identified as the *high proliferation index* (HPI) *tumor cells*. The subgroup containing cells with comparatively lower nucleus to cytoplasm ratio was named as *low proliferation index* (LPI) *tumor cells*. Regions exhibiting significant fibrosis were

classified into *early*, *intermediate* and *mature* fibrosis subgroups based on the maturity of the tumor's fibroplastic response. *Exudative necrosis*, necrosis marked by the presence of exudative fluids, and *focal necrosis*, spots of dead cells found within a viable tumor region, were the two types of necrotic regions observed in the measured samples

Results

Phantom Measurements

Since the scatter imager employed a confocal detection scheme, fluctuations in the sample plane's z-position could cause fluctuations in the measured signal. A homogeneous 5% IntraLipid™ phantom obtained by diluting a stock 20% IntraLipid solution (20% phospholipid-stabilized soy bean oil in water) was used to test the spatial uniformity of the scanner over a 1cm × 1cm scan area. Figures 2a and 2b show the average scattered irradiance image and its histogram. A batch of phantoms of varying volume concentrations of the stock IntraLipid solution was used to test the linear response of the system. The system response, as shown in Figure 2c, suggests that in the absence of absorption, the average irradiance of the remitted light is approximately proportional to the reduced scattering coefficient.

To test the probe's insensitivity to local absorption changes, another batch of IntraLipid phantoms was prepared with varying volume concentrations of whole animal blood. Heparinized whole animal blood harvested from a sheep was used and the IntraLipid concentration was fixed at 1% (μ_a=2.3×10^{-4} mm^{-1} and μ_s'=1.1 mm^{-1} at 633 nm, scaled from reported values for IntraLipid 10%)[35]. The estimated scatter parameters were expected to remain constant across this batch of phantoms despite the change in absorption. As expected, the average scattered irradiance and scattering power remained constant over increasing whole blood concentration as shown in Figure 2d. Estimated blood concentration index (*kc*) as shown in Figure 2e was negligible for low concentrations of blood. This behavior at low blood concentrations is expected to be due to the inherent insensitivity of the probe to local absorption. However for blood concentration values beyond 1% an approximately linear increase was observed. The estimated hemoglobin oxygen saturation fraction is shown in Figure 2f. It should be noted that the estimates of *d* are not reliable in phantoms with low concentration of blood due to the instrument's insensitivity to absorption under these conditions.

Tumor Measurements

Six pancreas and four prostate tumor samples were imaged using the scatter imaging system. The average scattered irradiance image and the scattering power images were extracted from the raw spectral images and are shown in Figures 3a-d. Figure 4 shows representative spectra acquired from pancreas and prostate tumor samples along with their corresponding empirical fits. Under the guidance of a veterinary pathologist several regions of interest corresponding to tissue types classified in Table 1 were identified on each of the measured tumor samples. Figure 5 shows an example where five regions-of-interest identified in a pancreatic tumor sample are shown overlaid on the scatter power image along with a close-up view (100x magnification) of the corresponding H&E sections. Region 1 shows HPI tumor cells with more cellular density compared to LPI tumor cells found in Region 2. Regions 3 and 4 show early and intermediate stages of fibrosis marked by the increased stromal content and less cellularity. Region 5 shows necrosis with the presence of exudative fluids and fragments of dead cells.

The average scattered irradiance and scatter power data for different tissue types were obtained by sampling corresponding histology guided regions-of-interest in the scatter images. Figures 6a and 6b show the grouped scatter plots of scattering power versus average scattered irradiance for pancreas and prostate tumor samples. Figures 7a and 7b show the box and whisker plots of average scattered irradiance and scatter-power distributions for different tissue types found in

the pancreas tumor samples. Figures 8a and 8b show the same for the prostate tumor samples. The boxes in these plots contain the "middle 50%" of the data distribution they represent, bounded by the first and the third quartiles. The line within the boxes represents the median (second quartile). The whiskers extend to 1.5 times the inter-quartile range from either end of the boxes. The notch around the median lines represents the 95% confidence interval within which the "true median" of the represented distribution exists. If the notches in two plotted distributions do not overlap, then one can conclude with 95% confidence that their true medians differ. The '+' symbols outside the whiskers indicate the outliers.

Discussion

The microsampling approach to spectroscopy applied here utilizes the local confinement of the signal to reduce the need for complex light transport modeling, which is often needed in deeper tissue signals. The confocal optical system confines the signal to approximately 100 μm laterally and to approximately a few hundred microns in the depth coordinate. The fitting used in equation 3, while empirical, has been found to be robust and a useful way to quantify scatter power from the remitted signal. The scatter power is independent of most coupling errors and uniquely associated with features related to the effective scatterer sizes [36-38]. A key feature in the design of this instrument has been to have a standard reference and acquire the spectrum in a referenced manner, so that measurements between samples could be compared directly for average value differences and for examination of the variation within a 'homogeneous' tissue type.

Despite this approach, it is believed that the remitted irradiance is perhaps a less reliable parameter than the scatter power, because this latter parameter is independent of coupling errors in the imaging system. Though all the spectral images acquired by the scatter imaging system were referenced to Spectralon to minimize referencing artifacts, the average scattered irradiance and scatter amplitude images were not entirely free from such artifacts due to small sample positioning and other instrumental issues. The increased "spread" in the average scattered irradiance compared to the scattering power as observed in Figures 6a and 6b is consistent with this behavior. As a result of this, high variance was observed in the average scattered irradiance box plots shown in Figures 7a & 8a. In addition to referencing issues, the scatter amplitude images also exhibited some coupling artifacts and hence were considered less reliable. However, the scatter power images were found to provide consistent trends across different tumor samples. This was due to the fact that scatter power relates to the slope of the wavelength dependent scatter function and hence is relatively free from referencing artifacts[39]. Still, interpreting the variation in scatter observed within a single tissue sample clearly indicates that the integrated scatter irradiance can vary up to 50% in most tumor samples, which is a level of heterogeneity which would be significant in optical therapies such as photothermal or photodynamic therapy. These imaging results can be used to better appreciate that there is a clear need for *in situ* light dosimetry in photodynamic therapy, since this high heterogeneity level will lead to significant variations in the tissue being treated. Further analysis of the effect that this variation has upon the transmitted light irradiance is clearly warranted.

However, for diagnostic purposes, one additional conclusion is that the scatter power may be a more reliable metric to compare between different samples, as it eliminates errors related to the coupling of the tissue to the microscope imager. The scattering power distributions of various tissue types plotted in Figures 7b and 8b were compared. The median scatter power of proliferative epithelium was found to be about 26% less than the same for mature epithelium in both pancreas and prostate tumor samples. It is well known that a significant portion of light scattered from tissue at higher scattering angles (>40°) comes from nuclear features and intracellular organelles in cytoplasm such as mitochondria [40-44], although recent work also

shows that the stroma between the cells can influence the scattering signature significantly[45]. Histopathology observations on the measured tissue types in this study revealed that LPI tumor cells exhibited higher cytoplasmic content and lower cell density, as compared to the HPI tumor cells which contained bigger nuclei and were more tightly packed. The higher organelle density per unit volume seen in mature tumor cells, due to increased cytoplasmic content, would clearly lead to higher scatter power as the number of small scattering features increases.

Exudative necrosis exhibited lowest scattering power response among all tissue types considered, with its median scatter power about 53% less than that of LPI tumor cells in pancreas tumor samples and 59% less in prostate tumor samples. This decrease has a physical explanation since the density of cells is significantly decreased and inflammatory infiltrate (edema, extracellular water or protein solute) occupies much of the space where tumor cells used to be. In comparison to *exudative* necrosis, regions of *focal* necrosis primarily contain mature tumor cells with spots of dead cells interspersed, and the scattering from these latter regions was similar to the mature tumor cell regions. The median scatter power of these two regions differed only by about 6%. Thus, the presence of the focal necrotic regions did not seem to have a significant reduction in the overall scatter. However based upon the reduction seen with exudative necrosis, it might be hypothesized that the scatter signal reduces in proportion to the fraction of cellular content within the region.

The prostate tumor samples only contained one region exhibiting significant mature fibrosis. The median scatter power in that region was about 13% lower than that of similar regions found in the pancreas tumor samples. Within the pancreas tumor samples, no significant difference in scatter power was observed between mature and early fibrosis regions. The intermediate fibrosis region was found to scatter more, with about 16% increase in the median scatter power. It is more challenging to interpret what these numbers mean, if anything, about how the morphology relates to the light scattering response. Since the changes are so subtle, it is likely difficult to quantify this further.

Finally, in all the measurements discussed above, the acceptance angle defined by the detection optical train limits the angular region sampled in the back-scatter geometry. So it should be noted that the scatter signal measured here is actually a complex mixture of both the scattering spectrum and the scatter phase function spectrum. Changes in the phase distribution of scattering could have significant influence on the discussed measurements. A comprehensive study on the effects of phase in these measurements would require discrete sampling of a significant portion of the back-scatter hemisphere and is beyond the scope of this study, although is being studied in set ups which are more conducive to this problem[44, 46-48]. Unfortunately the problem of measuring angularly resolved data from bulk tissue is complex, and so sampling of scatter from a narrow angle of collection is likely the only practical way to sample the scatter spectrum in thick tissues.

Conclusions

This study reports on the development and data collection from a raster-scanning confocal reflectance imaging system to directly quantify tissue scatter changes *in situ* with an attempt to interpret these changes relative to the tissue morphology. Phantom studies were conducted to validate the instrument performance and to demonstrate its insensitivity to local absorption changes. Finally, pancreas and prostate tumor samples were characterized using this instrument. The results, in combination with standard histopathology, demonstrate the instrument's capability to quantify scatter power, and that the scatter power appears correlated with the epithelial morphology. It is not clear how the signal to noise of imaging scatter power will compare to that of imaging average scattered irradiance. The latter is analogous to what would be seen by the human eye, but scatter power would be analogous to the color spectrum

of the scattered irradiance. The instrument is currently limited to *ex vivo* measurements due to inherent limitations of the sample scanning architecture and low scan speeds. The instrument's utility can be extended by moving to a beam scanning architecture that would be rapid, and hence more suitable for measurements in clinical settings.

Acknowledgments

The authors thank Dr. Xiaodong Zhou, Rendall R. Strawbridge, Imran Rizvi, Summer L. Gibbs-Strauss & Timothy Monahan for their help with the tumor models, sample preparation and histopathology related work. This work has been funded through NIH grants P01CA80139 and P01CA84203.

References

1. Kuroiwa T, Kajimoto Y, Ohta T. Development of a fluorescein operative microscope for use during malignant glioma surgery: a technical note and preliminary report. Surg. Neurol 1998;50(1):41–48. discussion 48-49. [PubMed: 9657492]
2. Bogaards A, Varma A, Collens SP, Lin A, Giles A, Yang VXD, Bilbao JM, Lilge LD, Muller PJ, Wilson BC. Increased brain tumor resection using fluorescence image guidance in a preclinical model. Lasers Surg. Med 2004;35(3):181–190. [PubMed: 15389738]
3. Ramella-Roman JC, Lee K, Prahl SA, Jacques SL. Design, testing, and clinical studies of a handheld polarized light camera. J. Biomed. Opt 2004;9(6):1305–1310. [PubMed: 15568952]
4. Demos SG, Radousky HB, Alfano RR. Deep subsurface imaging in tissues using spectral and polarization filtering. Opt. Express 2000;7(1):23–28. [PubMed: 19404365]
5. Yang VXD, Muller PJ, Herman P, Wilson BC. A multispectral fluorescence imaging system: design and initial clinical tests in intra-operative Photofrin-photodynamic therapy of brain tumors. Lasers Surg. Med 2003;32(3):224–232. [PubMed: 12605430]
6. Wilson, BC.; Patterson, MS.; Flock, ST.; Moulton, JD. The optical absorption and scattering properties of tissues in the visible and near-infrared wavelength range. In: Douglas, M.; Dall'Acqua, editors. Light Biol. Med. Plenum Publ.; 1988. p. 45-52.
7. Jacques SL. Time-Resolved Reflectance Spectroscopy in Turbid Tissues. IEEE Trans. Biomed. Eng 1989;36(12):1155–1161. [PubMed: 2606489]
8. Gratton E, Fantini S, Franceschini MA, Gratton G, Fabiani M. Measurements of scattering and absorption changes in muscle and brain. Phil. Trans. R. Soc. B 1997;352(1354):727–735. [PubMed: 9232861]
9. Cheong, WF. Summary of Optical Properties. In: Welch, AJ., editor. Optical-Thermal response of Laser-Irradiated Tissue. Plenum Press; New York: 1995. Appendix to Chapter 8
10. Sokolov K, Nieman LT, Myakov A, Gillenwater A. Polarized reflectance spectroscopy for pre-cancer detection. Tech. Canc. Res. Treat 2004;3(1):1–14.
11. Mourant JR, Johnson TM, Freyer JP. Characterizing mammalian cells and cell phantoms by polarized backscattering fiberoptic measurements. Appl. Opt 2001;40(28):5114–5123. [PubMed: 18364793]
12. Jacques SL, Roman JR, Lee K. Imaging superficial tissues with polarized light. Lasers Surg. Med 2000;26(2):119–129. [PubMed: 10685085]
13. Hielscher AH, Mourant JR, Bigio IJ. Influence of particle size and concentration on the diffuse backscattering of polarized light from tissue phantoms and biological cell suspensions. Appl. Opt 1997;36(1):125–135. [PubMed: 18250653]
14. Dam JS, Pedersen CB, Dalgaard T, Fabricius PE, Aruna P, Andersson-Engels S. Fiber-optic probe for noninvasive real-time determination of tissue optical properties at multiple wavelengths. Appl. Opt 2001;40(7):1155–1164. [PubMed: 18357101]
15. Bargo PR, Prahl SA, Jacques SL. Optical properties effects upon the collection efficiency of optical fibers in different probe configurations. IEEE J. Sel. Top. Quantum Electron 2003;9(2):314–321.
16. Utzinger U, Richards-Kortum RR. Fiber optic probes for biomedical optical spectroscopy. J. Biomed. Opt 2003;8(1):121–147. [PubMed: 12542388]

17. Mourant JR, Bocklage TJ, Powers TM, Greene HM, Bullock KL, Marr-Lyon LR, Dorin MH, Waxman AG, Zsemlye MM, Smith HO. In vivo light scattering measurements for detection of precancerous conditions of the cervix. Gynecol. Oncol 2007;105(2):439–445. [PubMed: 17303229]

18. Wilson BC, Jacques SL. Optical Reflectance and Transmittance of Tissues - Principles and Applications. IEEE J. Quantum Electron 1990;26(12):2186–2199.

19. Tromberg BJ, Svaasand LO, Fehr MK, Madsen SJ, Wyss P, Sansone B, Tadir Y. A mathematical model for light dosimetry in photodynamic destruction of human endometrium. Phys. Med. Biol 1996;41(2):223–237. [PubMed: 8746106]

20. Wilson BC, Patterson MS, Lilge L. Implicit and explicit dosimetry in photodynamic therapy: a new paradigm. Laser Med. Sci 1997;12(3):182–199.

21. Wax A. Low-coherence light-scattering calculations for polydisperse size distributions. J. Opt. Soc. Am. A 2005;22(2):256–261.

22. Wax A, Yang CH, Muller MG, Nines R, Boone CW, Steele VE, Stoner GD, Dasari RR, Feld MS. In situ detection of neoplastic transformation and chemopreventive effects in rat esophagus epithelium using angle-resolved low-coherence interferometry. Cancer Res 2003;63(13):3556–3559. [PubMed: 12839941]

23. Liu Y, Brand RE, Turzhitsky V, Kim YL, Roy HK, Hasabou N, Sturgis C, Shah D, Hall C, Backman V. Optical markers in duodenal mucosa predict the presence of pancreatic cancer. Clin. Cancer Res 2007;(15 Pt 1):4392–4399. [PubMed: 17671121]

24. Roy HK, Kim YL, Liu Y, Wali RK, Goldberg MJ, Turzhitsky V, Horwitz J, Backman V. Risk stratification of colon carcinogenesis through enhanced backscattering spectroscopy analysis of the uninvolved colonic mucosa. Clin. Cancer Res 2006;12(3 Pt 1):961–968. [PubMed: 16467111]

25. Kim YL, Turzhitsky VM, Liu Y, Roy HK, Wali RK, Subramanian H, Pradhan P, Backman V. Low-coherence enhanced backscattering: review of principles and applications for colon cancer screening. J. Biomed. Opt 2006;11(4):041125. [PubMed: 16965153]

26. Pogue BW, Hasan T. Fluorophore quantitation in tissue-simulating media with confocal detection. IEEE J. Quantum Electron 1996;2(4):959–964.

27. Pogue BW, Burke GC. Fiber optic bundle design for quantitative fluorescence measurement from tissue. Appl. Opt 1998;37(31):7429–7436. [PubMed: 18301577]

28. Weersink R, Patterson MS, Diamond K, Silver S, Padgett N. Noninvasive measurement of fluorophore concentration in turbid media with a simple fluorescence/reflectance ratio technique. Appl. Opt 2001;40(34):6389–6395. [PubMed: 18364948]

29. Amelink A, Sterenborg HJ. Measurement of the local optical properties of turbid media by differential path-length spectroscopy. Appl. Opt 2004;43(15):3048–3054. [PubMed: 15176191]

30. Amelink A, Sterenborg HJ, Bard MP, Burgers SA. In vivo measurement of the local optical properties of tissue by use of differential path-length spectroscopy. Opt. Lett 2004;29(10):1087–1089. [PubMed: 15181994]

31. Aphalo, P. Lamp Emission Spectra Database, Plant Photobiology Notes. 2007. retrieved 2008, >http://www.mv.helsinki.fi/aphalo/photobio/lamps.html

32. Prahl, SA. Oregon Medical Laser Center Website. retrieved 2007, http://omlc.ogi.edu/spectra/hemoglobin/

33. Zhou X, Pogue BW, Chen B, Hasan T. Analysis of effective molecular diffusion rates for verteporfin in subcutaneous versus orthotopic Dunning prostate tumors. Photochem. Photobiol 2004;79(4):323–331. [PubMed: 15137508]

34. Tennant TR, Kim HK, Sokoloff M, Rinker-Schaeffer CW. The dunning model. The Prostate 2000;43:295–302. [PubMed: 10861749]

35. Michels R, Foschum F, Kienle A. Optical properties of fat emulsions. Optics Express 2008;16(8): 5907–5925. [PubMed: 18542702]

36. Wang X, Pogue BW, Jiang S, Dehghani H, Song X, Srinivasan S, Brooksby BA, Paulsen KD, Kogel C, Poplack AP, Wells WA. Image Reconstruction of Effective Mie Scattering Parameters Of Breast Tissue In Vivo with Near-Infrared Tomography. J. Biomed. Opt 2006;11(4):041106. [PubMed: 16965134]

37. Bartek M, Wang X, Wells W, Paulsen KD, Pogue BW. Estimation of subcellular particle size histograms with electron microscopy for prediction of optical scattering in breast tissue. J. Biomed. Opt 2006;11(6):064007. [PubMed: 17212530]
38. Wang X, Pogue BW, Jiang S, Song X, Paulsen KD, Kogel C, Poplack SP, Wells WA. Approximation of Mie scattering parameters in near-infrared tomography of normal breast tissue in vivo. J. Biomed. Opt 2005;10(5):051704. [PubMed: 16292956]
39. Xu H, Pogue B, Springett R, Dehghani H. Spectral Derivative Based Image Reconstruction Provides Inherent Insensitivity to Coupling and Geometric Errors. Opt. Lett 2005;30(21):2912–2914. [PubMed: 16279467]
40. Beauvoit B, Kitai T, Chance B. Contribution of the Mitochondrial Compartment to the Optical-Properties of the Rat-Liver - a Theoretical and Practical Approach. Biophys. J 1994;67(6):2501–2510. [PubMed: 7696489]
41. Wilson JD, Giesselman BR, Mitra S, Foster TH. Lysosome-damage-induced scattering changes coincide with release of cytochrome c. Opt. Lett 2007;32(17):2517–2519. [PubMed: 17767290]
42. Wilson JD, Cottrell WJ, Foster TH. Index-of-refraction-dependent subcellular light scattering observed with organelle-specific dyes. J. Biomed. Opt 2007;12(1):014010. [PubMed: 17343485]
43. Wilson JD, Bigelow CE, Calkins DJ, Foster TH. Light scattering from intact cells reports oxidative-stress-induced mitochondrial swelling. Biophys. J 2005;88(4):2929–2938. [PubMed: 15653724]
44. Mourant JR, Canpolat M, Brocker C, Esponda-Ramos O, Johnson TM, Matanock A, Stetter K, Freyer JP. Light scattering from cells: the contribution of the nucleus and the effects of proliferative status. J. Biomed. Opt 2000;5(2):131–137. [PubMed: 10938776]
45. Arifler D, Pavlova I, Gillenwater A, Richards-Kortum R. Light Scattering from Collagen Fiber Networks: Micro-Optical Properties of Normal and Neoplastic Stroma. Biophys. J 2007;92:3260–3274. [PubMed: 17307834]
46. Cottrell WJ, Wilson JD, Foster TH. Microscope enabling multimodality imaging, angle-resolved scattering, and scattering spectroscopy. Opt. Lett 2007;32(16):2348–2350. [PubMed: 17700781]
47. Subramanian H, Pradhan P, Kim YL, Liu Y, Li X, Backman V. Modeling low-coherence enhanced backscattering using Monte Carlo simulation. Appl. Opt 2006;45(24):6292–6300. [PubMed: 16892135]
48. Canpolat M, Mourant JR. High-angle scattering events strongly affect light collection in clinically relevant measurement geometries for light transport through tissue. Phys. Med. Biol 2000;45(5):1127–1140. [PubMed: 10843095]

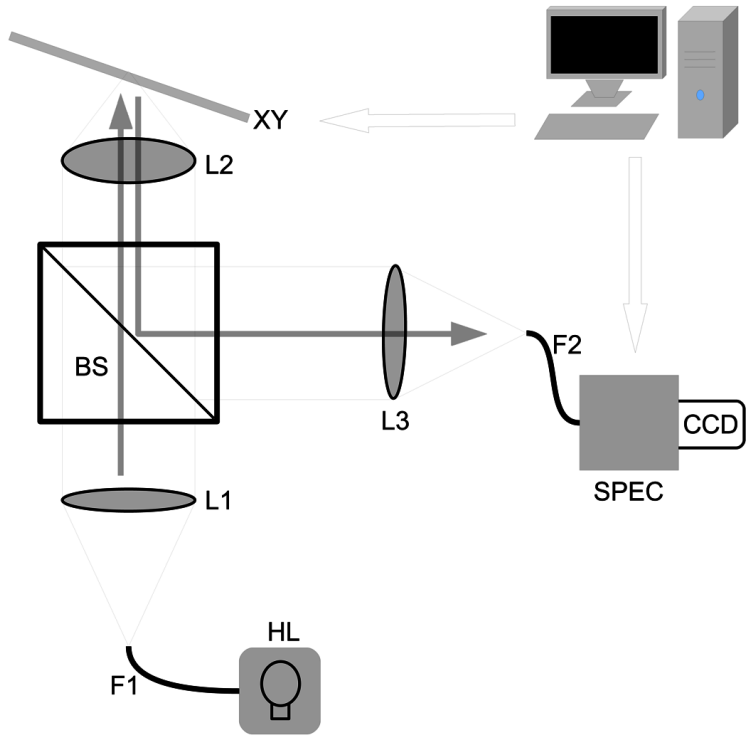

Figure 1.
Schematic of the raster-scanning scatter imager. The solid semi-transparent arrows show the illumination and detection beam paths. Identical achromatic lenses (L1 and L3), the objective lens (L2), the beam splitter (BS), the illumination fiber (F1) and the detection fiber (F2) are all arranged in the standard confocal geometry. The distal end of the detection fiber is coupled to a CCD based imaging spectrometer (SPEC), which records the remitted irradiance spectrum.

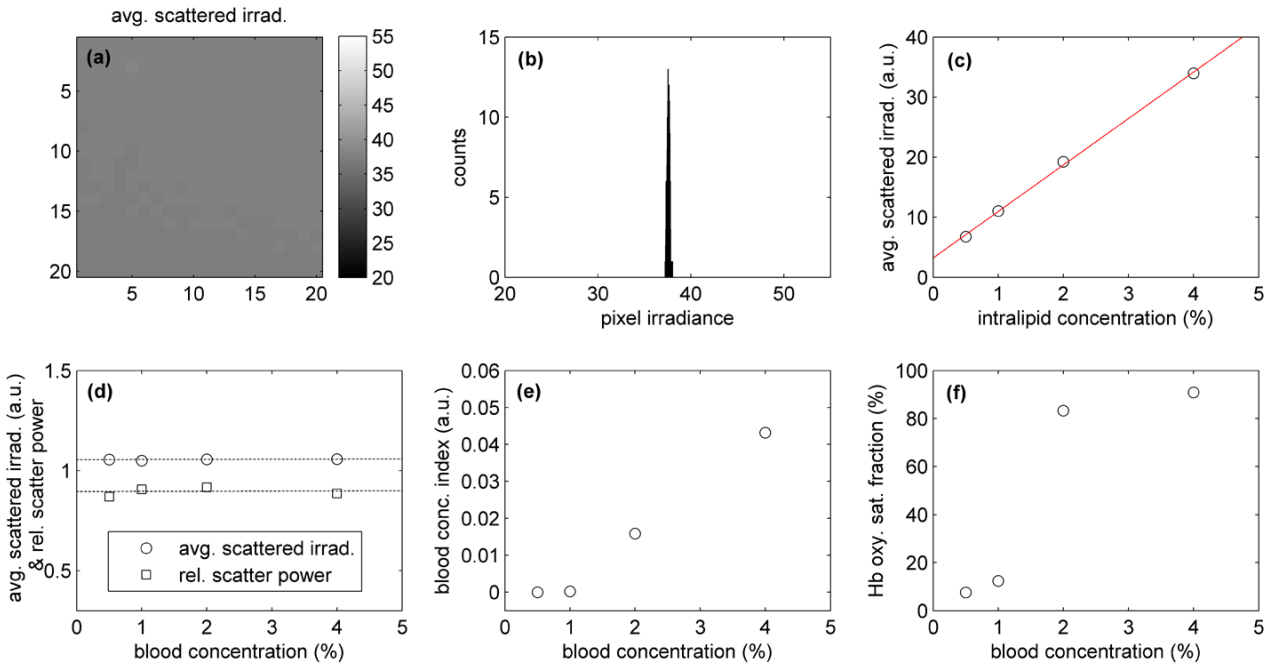

Figure 2.

(a, b) Average scattered irradiance image of a 1cm×1cm homogeneous 5% IntraLipid™ phantom and its associated histogram. (c) A plot of average scattered irradiance as a function of IntraLipid™ concentration. (d) Plots of average scattered irradiance (values scaled by a factor of 0.1) and scatter power as a function of blood concentration in a 1% IntraLipid™ phantom. The estimated scatter parameters are shown to be relatively independent of the changes in blood concentration. (e) Plot of estimated blood concentration index, *kc*, as a function of blood concentration. (f) Plot of estimated hemoglobin oxygen saturation fraction, *d*, in phantoms with different concentration of blood.

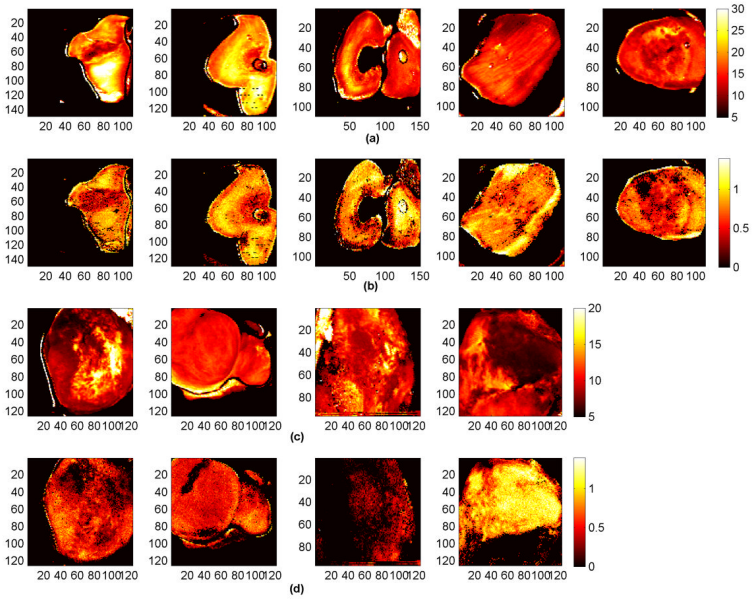

Figure 3.

(a & b) Average scattered irradiance and scatter power images of the measured pancreas tumor (AsPC-1) samples, the third image from the left contains two samples that were imaged together. (c & d) Average scattered irradiance and scatter power images of the measured prostate tumor (Mat-LyLu) samples.

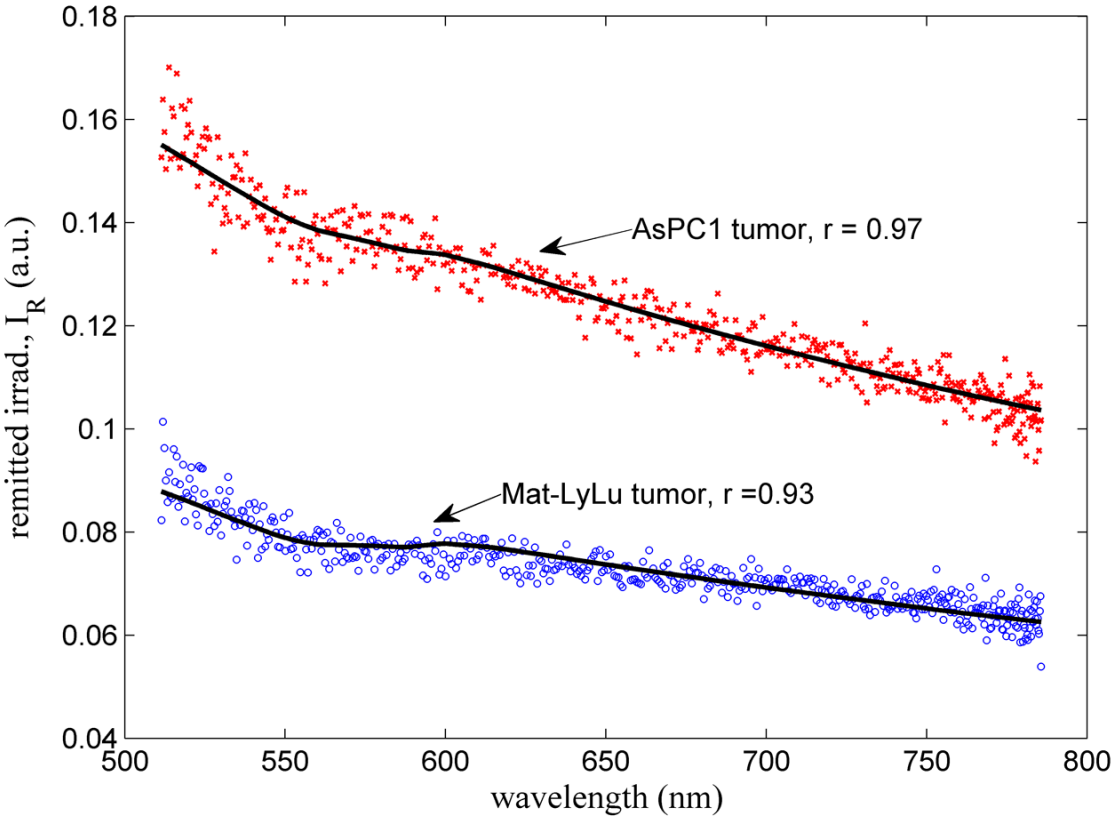

Figure 4.
Representative reflectance spectra measured in pancreas and prostate tumor samples along with their corresponding empirical fits to Equation 3 (solid line).

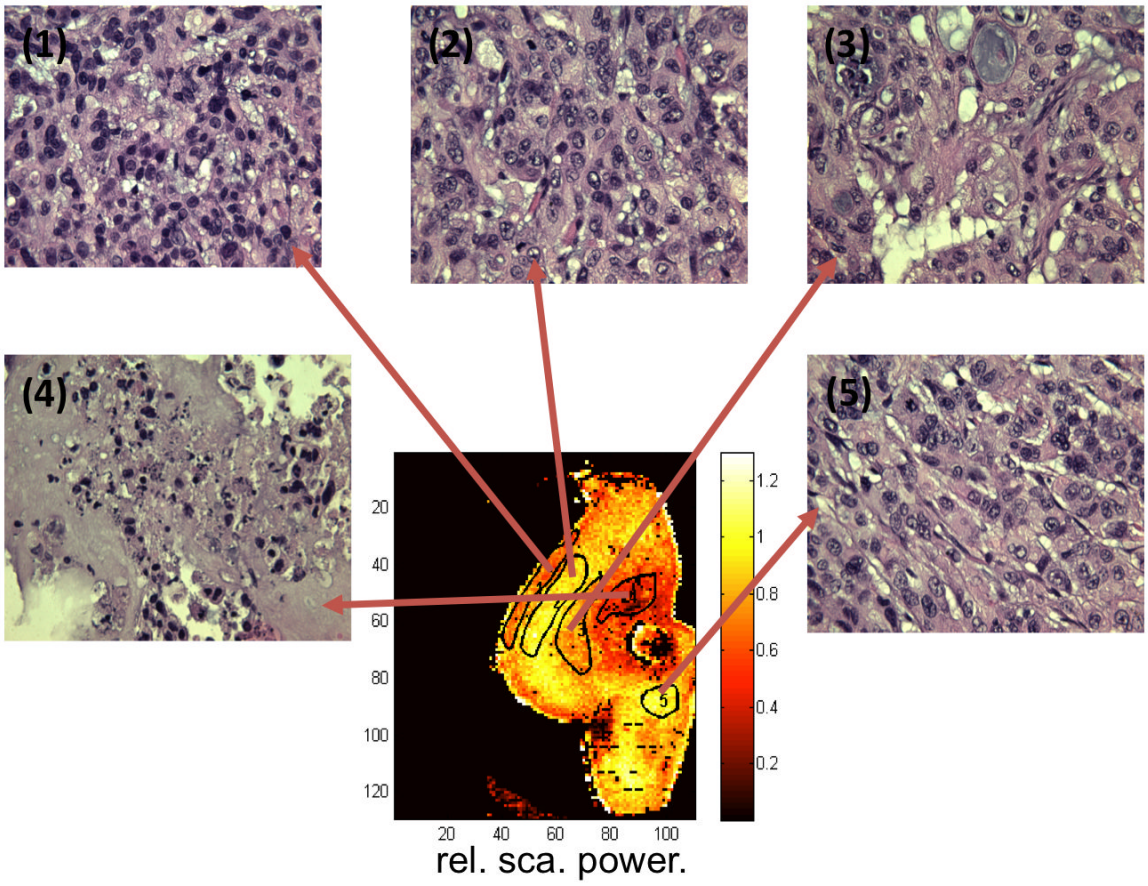

Figure 5.

The scatter power image of a pancreas tumor sample showing five pathology based regions-of-interest overlaid on it. Variations in tissue ultra-structure are evident on the shown high magnification (100x) pathology images: (1) High Proliferation Index (HPI) tumor cells, (2) Low Proliferation Index (LPI) tumor cells, (3) Significant Early fibrosis with some lipids, (4) Necrosis (exudative), and (5) Mature fibrosis.

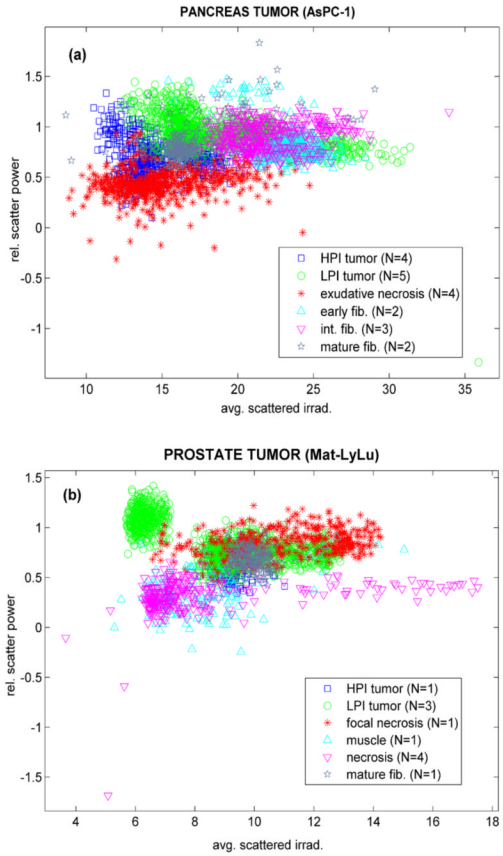

Figure 6.
(a & b) Grouped scatter plots of scattering power versus average scattered irradiance for all significant tissue types identified in pancreas and prostate tumor samples.

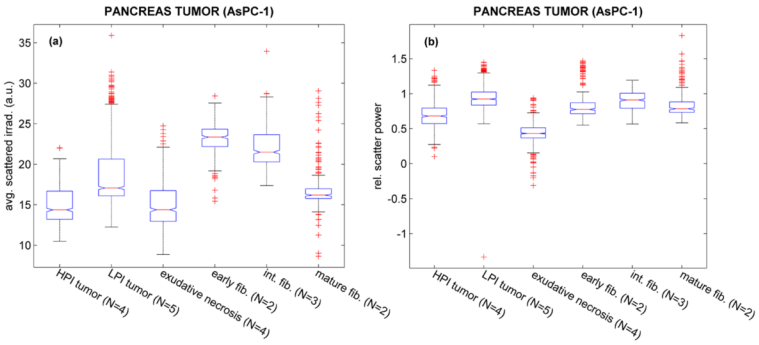

Figure 7.
Box and whisker plots of (a) average scattered irradiance and (b) scatter-power distributions, for all significant tissue types identified in pancreas tumor samples.

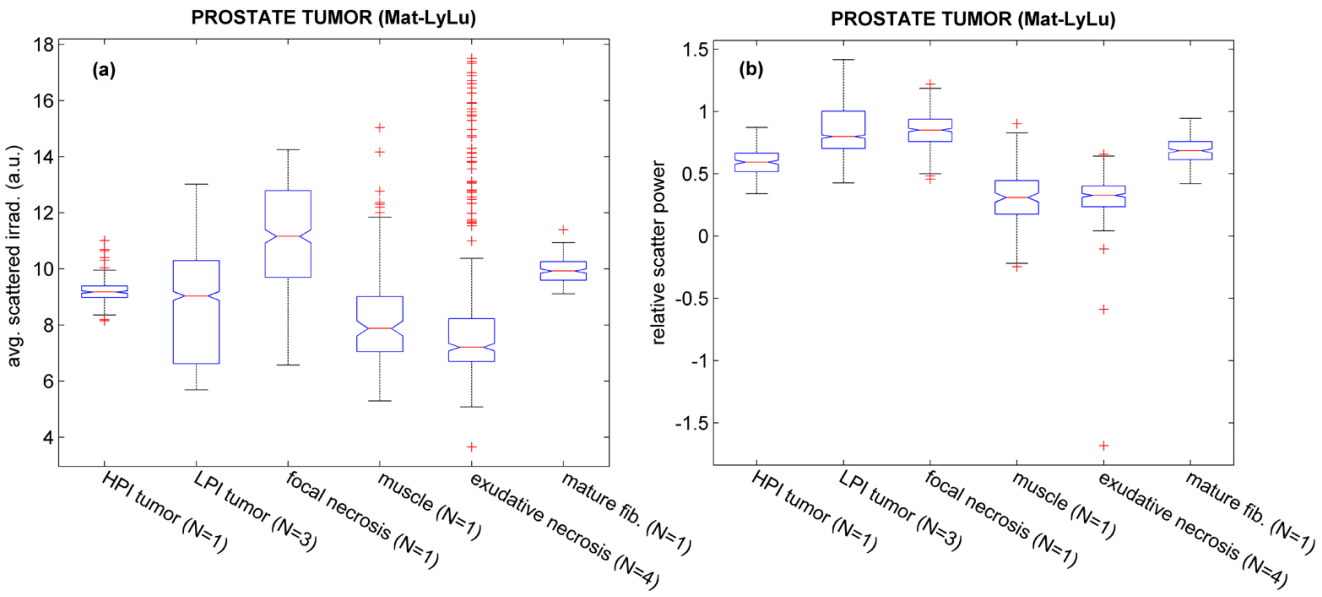

Figure 8.

Box and whisker plots of (a) average scattered irradiance and (b) scatter-power distributions, for all significant tissue types identified in prostate tumor samples. No regions corresponding to early and intermediate fibrosis were identified in the prostate tumor samples.

Table 1

Histopathology based classification of tissue sub-regions.

Group	Sub-groups
Epithelium	High Proliferation Index (HPI) tumor cells – High nucleus to cytoplasm ratio and high cellular density Low Proliferation Index (LPI) tumor cells – Lower nucleus to cytoplasm ratio and lower cellular density compared to HPI tumor cell regions
Fibrosis	Regions exhibiting significant fibrosis sub-classified based on the maturity of the fibroplastic response: Early fibrosis, Intermediate fibrosis and Mature fibrosis
Necrosis	Exudative necrosis – Exudate fluids with dead cells Focal necrosis – Spots of dead cells spread out in a viable tumor region